Estimating nitrogen stress and its impact on crop yield using advanced remote sensing approach

A case study of Gezira irrigation scheme, Sudan

Ahmed, Mahmoud H.; Pareeth, Sajid; Mul, Marloes

DOI
10.1016/j.jag.2025.104897

Publication date
2025

Document Version
Final published version

Published in
International Journal of Applied Earth Observation and Geoinformation

International Journal of Applied Earth Observation and Geoinformation 144 (2025) 104897

Contents lists available at ScienceDirect

International Journal of Applied Earth Observation and Geoinformation

journal homepage: www.elsevier.com/locate/jag

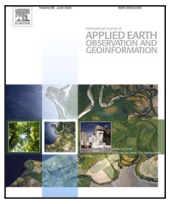

Estimating nitrogen stress and its impact on crop yield using advanced remote sensing approach: A case study of Gezira irrigation scheme, Sudan

Mahmoud H. Ahmed [a,*], Sajid Pareeth [c], Marloes Mul [b]

[a] Geoscience and Remote Sensing Department, Delft University of Technology, Delft, The Netherlands
[b] Land and Water Management Department, IHE Delft Institute for Water Education, Delft, The Netherlands
[c] Terra, Department of Education & Culture, Expo City Dubai, United Arab Emirates

ARTICLE INFO

Keywords:
Agricultural monitoring
Nitrogen content
Yield
Radiative transfer modeling
PROSAIL
Gaussian processes
Sentinel-2

ABSTRACT

Nitrogen (N) is crucial for crop and ecosystem health in agricultural settings. Traditional remote sensing (RS) methods, using regression models and indices like NDVI, face challenges in transferability across time and space. This study aims to enhance in-season N concentration assessment by integrating RS data with a hybrid approach, combining the PROSPECT-PRO and 4SAIL models to create PROSAIL-PRO. This Radiative Transfer Model (RTM) excels in parsing leaf protein, crucial for accurate crop N content estimation. PROSAIL-PRO forms the basis for a robust learning database, guiding the training of Gaussian Process Regression (GPR) models—Bayesian-based machine learning known for precision and insights into uncertainties. The Gezira irrigation scheme in Sudan serves as a case study. Using Sentinel-2 bands, this research informs agricultural resource management and assesses crop health in the scheme. Fertilizer application data and yield records drawn from three farms within the Gezira scheme to form the basis for validation. Wheat, the primary crop in this context, experienced varying fertilizer application scenarios across these farms during the 2021-22 cropping season resulting in varying yields. Similar results were found in the crop N content and biomass estimation. GPR models, trained on PROSAIL-PRO, effectively predict above ground N content and biomass. Validation against field records shows promising outcomes, with GPR models exhibiting an RMSE of 7.9 kg/ha for N content and 0.54 tonnes/ha for yield estimation. Moreover, the model's spatiotemporal scalability was assessed, showing an RMSE of 1.01 tonnes/ha at the Nimra level and 1.6 tonnes/ha at the farm level, highlighting the applicability of this approach to larger areas. A significant correlation (0.7) was found between estimated N concentration and actual recorded yield at the field level, further corroborated by an 0.83 correlation at the Nimra level. These results emphasize the robustness of this hybrid modeling approach, particularly in linking nitrogen dynamics to primary productivity, as evidenced by stronger correlations between NPP and nitrogen content than between N content and fAPAR. This study therefore highlights the benefits of adoption hybrid modeling, based on PROSAIL-PRO, in global agricultural monitoring. The synergy found between remote sensing, radiative transfer modeling, and real-world dynamics promises a sustainable future for agriculture applications.

1. Introduction

The challenge of ensuring food security is becoming increasingly pressing due to rising demands for food and freshwater supplies, alongside the backdrop of climate variability and change. This interdependence between water resources and food security has been underscored by the Food and Agricultural Organization of the United Nations (FAO), recognizing that actions taken in one domain can profoundly affect the other. Such efforts are vital for enhancing human well-being, alleviating poverty, and fostering sustainable development (FAO, 2014). Thus, the imperative to continuously enhance water and land productivity to sustain food security persists as a critical endeavor for both present and future generations (Safi et al., 2022).

Agriculture serves as the fundamental backbone of human existence and exerts considerable influence on economic dynamics (Ennouri and Kallel, 2019). Consequently, it becomes paramount to carefully track the state of crops throughout their developmental stages. This involves evaluating a spectrum of factors including nutritional parameters, soil moisture content, plant vigor, and susceptibility to stressors stemming from both abiotic (e.g., humidity, temperature) and biotic (e.g., pests and diseases) sources (Ennouri and Kallel, 2019). Any departure from the optimal parameters during each growth phase can have

* Corresponding author.
E-mail address: m.ahmed@tudelft.nl (M.H. Ahmed).

https://doi.org/10.1016/j.jag.2025.104897
Received 29 April 2024; Received in revised form 27 July 2025; Accepted 7 October 2025
Available online 14 October 2025

adverse effects on crop development, leading to reduced production and productivity.

Nitrogen (N) holds pivotal significance in agriculture, being indispensable for the well-being of plants, animals, and soil ecosystems. Within the soil, nitrogen exists in diverse forms, undergoing frequent transformations from one form to another (Science of Agriculture, 2017). *N* deficiency can exert a substantial impact on various aspects of plant physiology, including leaf chlorophyll content and photosynthesis rate, thereby influencing plant development and ultimately reducing biomass production (Mu and Chen, 2021). The decline in leaf photosynthesis rate attributed to *N* deficiency primarily stems from decreased stomatal conductance, rather than a diminished capacity for carboxylation within the leaf structure (Zhao et al., 2005).

Precision agriculture (PA) stands out for its emphasis on augmenting farmers' comprehension of their fields and crops, offering substantial benefits in terms of heightened productivity and optimized input employment (Gebbers and Adamchuk, 2010). Complementing PA, Variable Rate Technology (VRT) plays a pivotal role by enabling the targeted application of farm inputs, such as fertilizer and water, at varying rates across the field, guided by site-specific data (He, 2022). Further refining this approach, Variable Rate Fertilization (VRF) emerges as an advanced PA technique, leveraging embedded high-speed computers, remote sensing (RS) technologies, Geographic Information Systems (GIS), precise Global Positioning System (GPS) receivers, soil maps, alongside real-time crop characteristics measurement and prediction capabilities through electronic sensors and actuators (Schumann, 2010). VRF methodologies harbor the potential to augment fertilizer use efficiency, mitigate environmental impacts, and refine both crop quality and yield outcomes (Gao and Li, 2022).

Remote sensing (RS) products have a critical role in the development of decision support tools for PA and VRF, employing sophisticated sensor and analysis tools to enhance crop yields and facilitate management decisions (Singh et al., 2020). Recent advancements have seen the integration of PA technologies based on RS into commercial farming practices (Sishodia et al., 2020). The integration of VRF with prescription maps is recognized as a promising strategy for achieving targeted top-dressing fertilization, thereby enhancing nitrogen application efficiency (Basso et al., 2016). To facilitate this, variable rate maps can be generated by leveraging various thematic layers as inputs for classical or unsupervised clustering algorithms, thereby delineating site-specific management zones (Fridgen et al., 2003).

RS techniques offer a versatile means to estimate various parameters, ranging in complexity, which serve as indicators of the nitrogen status of crops. *N* content in plants often exhibits correlations with wavelengths similar to those of chlorophyll (Chl) (Rubo and Zinkernagel, 2022). Notably, as water content decreases, reflectance tends to increase, with significant information regarding water content being encoded in key wavelengths such as 1450, 1940, and 2500 nm (Jacquemoud and Ustin, 2019). The significant absorption resulting from water in the reflectance spectra of fresh leaves can obscure the relatively weaker absorption associated with plant biochemical components, such as nitrogen absorption features (Kokaly, 2001).

Many models have been developed to simulate the propagation of electromagnetic radiation through both the atmosphere and vegetation canopies, taking into account the structural and inherent properties of crops to accurately forecast the transmission of radiation (Chen et al., 2017). The utilization of such models typically entails either directly employing the retrieved variables as input for the model (e.g., LAI, dry mass, and leaf chlorophyll content) or simulating the variable within the model (e.g., green fraction, photosynthetically active radiation (PAR) - fraction absorbed by green vegetation (fAPAR)) (Weiss et al., 2020). Radiative Transfer Models (RTM), which are physically-based models, have been leveraged for nitrogen retrieval (Berger et al., 2018; Li et al., 2018, 2019; Wang et al., 2018). RTMs explain the interaction of photons with the biophysical and biochemical attributes of plants and find extensive applications in remote sensing, encompassing the inversion of parameters from satellite bands, the development of parametric and nonparametric regression techniques, and the integration of machine learning (ML) regression methods with RTM simulations in hybrid regression approaches (Verrelst et al., 2019).

While conventional methodologies, such as regression models developed using indices like NDVI and in-situ crop biophysical data, have been widely applied, their transferability across different temporal and spatial contexts is often limited (Kang et al., 2016; Ali et al., 2016). Recent studies have highlighted these challenges (Mridha et al., 2021), emphasizing the need for more robust alternatives. This study, therefore, focuses on a novel approach that addresses these limitations by leveraging physical models based on RTM, which have been proven to be more robust, transferable, and accurate in retrieving crop biophysical and biochemical parameters (Mridha et al., 2014; Sehgal et al., 2013, 2016; Upreti et al., 2019; Bacour et al., 2006). The major limitations of this approach include the ill-posed problem, where different combinations of biophysical and biochemical parameters can produce similar reflectance values, and the relatively slow computational speed compared to other methods.

This research aims to assess nitrogen concentration in agricultural fields throughout the cropping season by leveraging RS data and RTMs. The integration of these technologies offers a novel approach to estimate crucial variables related to soil fertility and crop nutrition. The specific objectives include exploring the potential of capturing key variables using satellite data, evaluating the accuracy of nitrogen level retrieval and biomass estimation for a selected crop through a machine learning model trained on simulated reflectance at the canopy level, assessing the impact of nitrogen levels on crop yield at the season's conclusion, and testing the spatiotemporal transferability of the produced models. By addressing these objectives, this study seeks to contribute valuable insights into the application of remote sensing and machine learning for precision agriculture, bridging existing knowledge gaps in the utilization of these techniques for optimizing crop management practices. Given the importance of the Gezira Scheme as one of the largest irrigation initiatives globally—historically contributing to 60% of Sudan's total wheat production from 1980 to 1990 (Elsayed et al., 2019), this research is especially relevant for promoting sustainable practices within extensive irrigation systems.

2. Materials and methods

2.1. Study area

The Gezira Scheme, situated south of Khartoum, the capital of Sudan, encompasses Al Gezira State. As depicted in Fig. 1, the scheme is divided into four main divisions. Nestled between the Blue Nile and White Nile rivers, the Gezira Scheme constitutes a significant agricultural area boasting extensive irrigation infrastructure. The Sennar dam and reservoir in the Blue Nile serve as the command level for the scheme's gravity flow-based irrigation canals. Managed by a singular governing body, the scheme stands as one of the world's largest irrigation projects (Hussein et al., 2002). Covering approximately 882,400 hectares (2.1 million feddans), the Gezira Scheme surpasses the combined size of all projects in the Blue Nile river basin, such as Asalaya and Rahad. Wheat emerges as one of the primary crops cultivated within the scheme, typically sown in early to mid-November and harvested 110–120 days post-sowing, with an estimated yield ranging from 0.85 to 1.0 tonnes/feddan (2.02–2.38 tonnes/ha) (Elkhidir, 2019).

This study focused on three wheat-cultivating farms located in the southern sector of the Gezira Scheme, within the Musalamia administrative unit of the project area (Fig. 2). Fieldwork was carried out during the 2021–22 cropping season, and the selection of farms was guided by the availability of relevant data. A key consideration in the selection was that the farmer had implemented an experimental trial during the season, applying three separate fertilization regimes across the three farms (details provided in Table 1). The final yield achieved

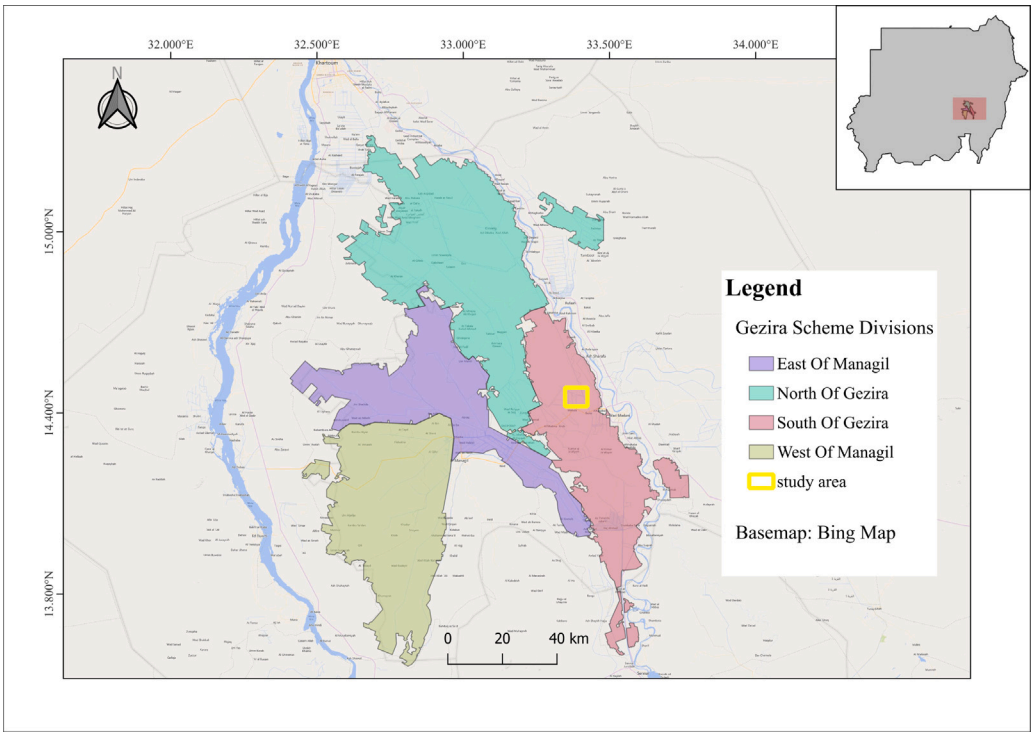

Fig. 1. Gezira irrigation scheme main divisions.

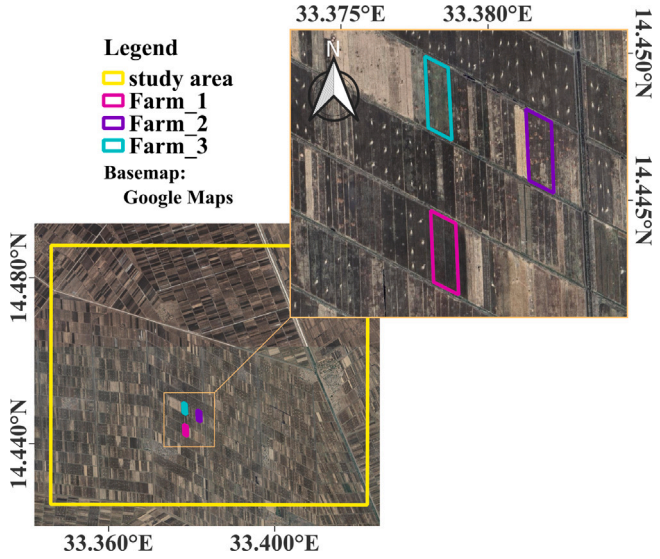

Fig. 2. The three wheat farms in southern part of Gezira Scheme.

at the end of the season served as the main criterion for determining the most effective fertilization strategy.

In this experiment, the process started with land ploughing at the beginning of October, preparing the ground for the subsequent sowing period (which occurred after 45 days). During this phase, varying levels of Di-ammonium Phosphate (DAP) were applied across the three farms (as detailed in Table 1). Notably, Farm-1 utilized Single Super Phosphate (SSP) in conjunction with DAP. Following these initial stages, the first irrigation was typically applied between the 15th and 20th of November. As the season progressed, a total of eight irrigation events were administered, each spaced 12 days apart. Urea application took place from the second to the fifth irrigation, with each application amounting to 59.5 kg/ha. Ultimately, the crop reached maturity 100 days after the first irrigation, indicating its readiness for harvest.

To test the Spatiotemporal transferability of the trained models an analysis was conducted for a different subzone in the Gezira scheme, namely called Wad-Hilal area, more specifically, the focus was on eight tertiary units (named hereafter as Nimras) during the 2022–23 Winter season (see Fig. 3). During that season, these eight Nimras had a total of 214 Wheat-cultivating farms all of which had a record of the final yield collected by HRC as part of Elnour (2023) research.

2.2. Experimental setup

Fig. A.16 provides an overview of the methodology employed in this study. The core analysis for the study covered a wider area, demarcated by the yellow boundary in Fig. 2, which included the three farms of interest.

2.2.1. RTM

The process of radiative transfer modeling begins with the random generation of 21,000 distinct points, each comprising a set of 14 biophysical and biochemical variables (BV) values representing PROSPECT and SAIL parameters. These input points were independently created outside the model and thoroughly designed to align with the specified statistical properties of the parameters and their relationship with LAI. Before proceeding with further steps, a sensitivity analysis was conducted to evaluate the connection between the simulated reflectance and various factors, including LAI, Cp, sun zenith angle (SZA), viewing zenith angle (VZA), and Relative Sensor-Solar Azimuth Angle (psi). The selection of relevant Sentinel-2 (S2) bands was based on the outcomes of this sensitivity analysis. Subsequently, the fraction of absorbed photosynthetically active radiation (fAPAR) and canopy reflectance were simulated across all input configurations. The simulated canopy reflectance values were then adjusted to match S2-specified bands using the Sentinel-2 Spectral Response Function (S2-SRF).

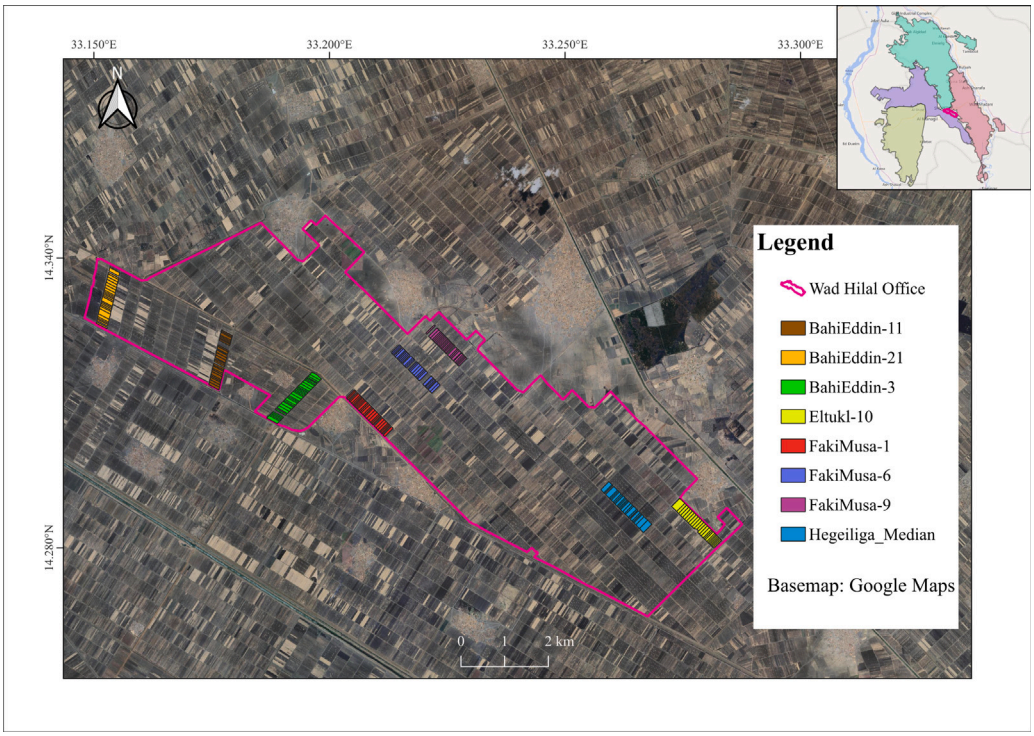

Fig. 3. Wad Hilal subzone and the eight tertiary units.

Table 1
Farm management strategies during the 2021-22 season.

Parameter	Farm-1	Farm-2	Farm-3
Area in Feddan (Hectare)	6 (2.52 ha)	6 (2.52 ha)	6 (2.52 ha)
Sowing amount (kg/ha)	143	143	143
Land Preparation Fertilizer (kg/ha)	119 DAP + 119 SSP	119 DAP	178 DAP
Urea (kg/ha)	238	238	238
Yield (tonnes/ha)	3.4	2.9	4.2

2.2.2. Machine learning

The aforementioned process yielded an extensive database, which was subsequently divided into two subsets for training and validation purposes. Each subset comprised paired data, consisting of simulated reflectance and nitrogen content for training the nitrogen Gaussian Process Regression (GPR) model, and simulated reflectance and fAPAR for the fAPAR GPR model. The choice of GPR was further supported by the findings of Upreti et al. (2019), who compared various machine learning algorithms and concluded that Gaussian Processes outperformed others during cross-validation for estimating classical biochemical and biophysical variables. The decision to generate 21,000 points for this database was informed by insights from available literature and a systematic trial-and-error approach. Of the total 21,000 points, 14,000 were allocated for training, a number deemed sufficient to achieve robust training performance, surpassing the minimum requirement of 10,000 points suggested for a medium complexity problem by Weiss and Baret (2016). This approach aimed to strike a balance between data size and time efficiency for both training and prediction tasks.

Considering that Gaussian Processes entail computationally intensive processes, the training of both models *N* GPR and fAPAR GPR took place within the Google Colab cloud environment, leveraging the computational capacity of an NVIDIA A100 Tensor Core GPU with 40 GB VRAM. Each model underwent 10,000 training iterations, followed by validation using 7000 testing data points. During validation, metrics such as Root Mean Square Error (RMSE) and R-squared (R2) were computed to assess the models' adherence to the dataset.

2.2.3. Prediction and validation

For this study, S2 images covering all of the 2021–22 cropping season were acquired and subsequently clipped to the boundaries of the study area. The trained GPR models were then applied to the ten S2 bands to predict *N* and fAPAR across the entire study area, as illustrated in Fig. 2. Subsequently, the fAPAR predictions were used to calculate Net Primary Production (NPP) for the study area. Following this prediction phase, the anticipated values underwent a comparative validation assessment, wherein they were compared against the actual field measurements recorded during the 2021–22 growing season for the three farms under investigation. Finally, the time series of nitrogen concentrations, along with the corresponding estimates of biomass, were utilized in conjunction with a selected Wheat Nitrogen dilution curve to determine the application rate of nitrogen fertilization and assess its alignment with the crop's needs throughout the growing season.

2.2.4. Spatial and temporal transferability

To evaluate the model's ability to operate across diverse locations and timeframes, a spatiotemporal transferability assessment was conducted during the 2022–23 winter season. This assessment involved running the trained GPR models to predict *N* concentration and fAPAR over the eight Nimras in the Wad Hilal unit (Fig. 3). Subsequently, the correlation between the estimated nitrogen concentration and both the modeled and actual recorded yield was computed.

Table 2
PROSAIL input parameterization for creating Sentinel-2 reflectance used for GPR training.

Parameter	Abbrev.	(unit)	Distribution law	Min	Max	SD	Mode	Ref.
PROSPECT-PRO:								
Leaf protein content	C_p	(g/cm^2)	Gaussian	0.001	0.0025	0.0005	0.00175	Berger et al. (2020)
Leaf chlorophyll a + b content	C_{ab}	(μg/cm^2)	Gaussian	20	90	30	45	Delloye et al. (2018)
Leaf structure parameter	n	(no dim.)	Uniform	1.3	2.5	–	–	Verrelst et al. (2016)
Equivalent water thickness	C_w	(cm)	Uniform	0.002	0.05	–	–	Rivera et al. (2013)
Leaf carotenoid content	C_{car}	(μg/cm^2)	Gaussian	0	15	3	7	Berger et al. (2020)
Leaf anthocyanin content	C_{anth}	(g/cm^{-2})	Gaussian	0	2	0.3	1	Berger et al. (2020)
Brown pigment content	C_{brown}	(no dim.)	Gaussian	0	2	0.3	0	Delloye et al. (2018)
Carbon-based constituents	C_{bc}	(g/cm^2)	Gaussian	0.001	0.01	0.0015	0.005	Berger et al. (2020)
Leaf mass per area	C_m	(g/cm^2)	Uniform	0.001	0.03	–	–	Rivera et al. (2013)
4SAIL:								
Leaf area index	LAI	(m^2/m^2)	Gaussian	1	8	2	2	Rivera et al. (2013)
Average leaf inclination angle	lidfa	(°)	Uniform	30	80	–	–	Delloye et al. (2018)
Hotspot parameter	hspot	(m/m)	Uniform	0.05	0.5	–	–	Richter et al. (2011)
Soil brightness	rsoil	(no dim.)	Uniform	0	1	–	–	Berger et al. (2020)
Soil moisture	psoil	(no dim.)	Uniform	0	1	–	–	–
Sun zenith angle	SZA	(°)	–	40°				–
View zenith angle	VZA	(°)	–	0°				–
Sun-sensor azimuth angle	psi	(°)	–	0°				–

2.3. Data

2.3.1. Generating the learning database

The selection of appropriate ranges for the biophysical and biochemical variables (BV) is crucial for ensuring the accuracy of forward simulation in PROSAIL. Careful consideration of these ranges is essential to ensure that the simulated reflectance accurately captures meaningful features of the BV. Consequently, when creating the training dataset for the Gaussian Process (GP) model, it is imperative to choose parameter ranges that mitigate the potential ill-posed problem. Therefore, for each input parameter, the typical range and distribution are determined (Table 2 lists the input parameters for the PROSAIL model, along with notations, units, and the range of parameters).

To establish a relationship between BV and LAI, we adopted a concept introduced by Weiss and Baret (2016). According to this concept, the dynamics of parameters vary linearly with LAI, and these changes are constrained by new limits defined as Vmin(LAImin), Vmax(LAImin), Vmin(LAImax), and Vmax(LAImax). These modified limits are illustrated in Table 3, providing a clearer understanding of how parameter values evolve in response to variations in LAI compared to their original boundaries. Specifically, as LAI transitions from LAImin to LAImax, the BV range undergoes adjustments within linear upper and lower limits that extend from Vmax(LAImin) to Vmax(LAImax) and from Vmin(LAImin) to Vmin(LAImax), respectively. This approach enables a finer characterization of parameter behavior across the entire LAI range, thereby enhancing the accuracy and reliability of our modeling framework.

Following the generation of PROSAIL simulations, adjustments were made to match the actual spectral response of Sentinel-2 (S2) using the latest Sentinel-2 Spectral Response Function (S2-SRF). Additionally, while fAPAR is not a primary input parameter, it was simulated by running the same input parameters for all generated reflectance values. Subsequently, the training database was divided into two segments: two-thirds were designated for training the Gaussian Process (GP) model, while one-third was allocated for validation.

2.3.2. Sentinel-2

The Copernicus Sentinel-2 (S2) mission provides spectral reflectance data with frequent revisits every 5 days, fine spatial resolution (10 m), comprehensive global coverage, and an open access policy (Gascon et al., 2017). These attributes collectively position it as an invaluable resource for the development of near-real-time operational agricultural services (Delloye et al., 2018). In this study, the level two product (L2A) of the multispectral instrument (MSI) was utilized to acquire the S2 mission tiles with relative orbit number 078 and tile number 36PWB across the targeted cropping season from November 2021 to February 2022 (Table 4). The L2A data undergoes atmospheric correction through the Sen2Cor processor, eliminating the need for additional correction steps and enhancing the reliability of the reflectance values used in our analysis. Cloud cover for all images remained well below the 20% threshold. Subsequently, the acquired L2A products were clipped to match the study area (Fig. 2) and were transformed from digital numbers to reflectance values at 10 m resolution using the semi-automatic classification plugin in QGIS (Congedo, 2021). This processing resulted in a set of 10 bands that will serve as inputs for predicting nitrogen content and fAPAR. The selection of these specific bands was guided by their robust correlation with plant nitrogen content and biomass estimation. Notably, prior research highlights the significance of certain bands in these estimations. For instance, Guerif et al. (2007) demonstrated the feasibility of assessing nitrogen concentration through spectral features in visible and Red-edged bands, which are indicative of chlorophyll content.

Similarly, Berger et al. (2020) advocated for the utilization of the short-wave infrared (SWIR) spectral domain to estimate nitrogen levels through the proxy of proteins. In this context, the results of the sensitivity analysis, combined with insights from existing literature, was leveraged to determine the optimal bands for estimating nitrogen concentration and biomass.

Table 3
Statistical properties of the PROSAIL input parameters.

Parameter	Vmin(LAImin)	Vmax(LAImin)	Vmin(LAImax)	Vmax(LAImax)
C_p	0.001	0.0025	0.0019	0.001
C_{ab}	20	90	45	90
n	1.3	2.5	1.4	2
C_w	0.002	0.05	0.004	0.05
C_{ar}	0	15	0.1	0.5
C_{anth}	0	2	0	2
C_{brown}	0	2	0	2
C_{bc}	0.001	0.01	0.003	0.01
C_m	0.001	0.03	0.005	0.03
LAI	–	–	–	–
lidfa	30	80	55	65
hspot	0.05	0.5	0.05	0.5
rsoil	0	1	0	0.2
psoil	0	1	0	1

2.4. PROSAIL-PRO configuration

2.4.1. N content estimation

In this study, a Python version of PROSAIL-PRO (Domenzain et al., 2019) was employed to generate a lookup table (LUT) to serve as a

Table 4
S2-MSI-L2A Acquired data for 2021-22 season.

Sensing date	Platform	Cloud cover %
2021–11–23	A	0.0
2021–11–28	B	0.0
2021–12–03	A	0.0
2021–12–08	B	0.0
2021–12–13	A	1.4
2021–12–18	B	0.0
2021–12–23	A	1.5
2021–12–28	B	0.0
2022–01–07	B	0.3
2022–01–12	A	2.9
2022–01–17	B	0.9
2022–01–22	A	3.4
2022–01–27	B	1.5
2022–02–01	A	0.0
2022–02–06	B	4.9
2022–02–11	A	2.7
2022–02–16	B	7.0
2022–02–21	A	0.0
2022–02–26	B	0.4

training database. Operating collaboratively, this coupled model simulates canopy-scale reflectance, predicted from a diverse set of biophysical parameters (such as Leaf Area Index (LAI) and average leaf inclination angle) as well as leaf biochemical inputs (including leaf Chlorophyll-a+b content (C_{ab}), equivalent water thickness (C_w), and leaf carotenoid content (C_{ar}). The direct calculation of leaf nitrogen content (N_a) from leaf protein content (C_p) is facilitated through the protein-to-nitrogen conversion factor of 4.43 (Wang et al., 2018), as established by Yeoh and Wee (1994) after studying 90 plant species. This factor is utilized according to the equation below:

$$N_a = \frac{C_p}{4.43}\left(\frac{\mathrm{g}}{\mathrm{cm}^2}\right) \tag{1}$$

Moreover, in the transition from the leaf level to the canopy scale, LAI served as an upscaling parameter. This enabled the calculation of above-ground nitrogen content from the entry points in the LUT, utilizing LAI and leaf protein content (C_p) for each input point, as recommended by Berger et al. (2020), outlined as follows:

$$\text{above ground N content}\left(\frac{\mathrm{g}}{\mathrm{m}^2}\right) = N_a\left(\frac{\mathrm{g}}{\mathrm{cm}^2}\right) \times \mathrm{LAI}\left(\frac{\mathrm{m}^2}{\mathrm{m}^2}\right) \times 10{,}000 \tag{2}$$

2.4.2. fAPAR simulation

In the domain of canopy radiative transfer, the computation of fAPAR encompasses multiple elements. This involves the direct absorption of radiation by the canopy ($a_1(\lambda)$), along with the fraction reflected by the background and subsequently absorbed by the vegetation ($a_2(\lambda)$). Consequently, the total energy absorbed by the green canopy can be expressed by the equation:

$$a(\lambda) = a_1(\lambda) + a_2(\lambda) \tag{3}$$

Here, λ denotes the wavelength. The determination of $a_1(\lambda)$ rests upon the assumption of negligible background reflectance (r_g). In this context, the instantaneous fAPAR can be expressed as:

Here, λ denotes the wavelength. The calculation of $a_1(\lambda)$ is predicated on the assumption of negligible background reflectance (r_g). In this context, the instantaneous fAPAR can be formulated as:

$$fAPAR = \int_{0.4\,\mu\mathrm{m}}^{0.7\,\mu\mathrm{m}} a(\lambda)\,d\lambda \tag{4}$$

This conceptual framework is adapted from (Fan et al., 2014). In the core of the computation of fAPAR within this framework are a series of critical parameters, which are either directly calculated or derived as secondary quantities within the SAIL model. The SAIL parameter for the fraction of diffuse incoming solar radiation (skyl) incorporates the Solar Zenith Angle (SZA) (François et al., 2002), which is based on an average atmospheric condition representative of mid-latitudes. The calculation of skyl is expressed as:

$$skyl = 0.847 - 1.61\sin(90° - \mathrm{SZA}) + 1.04\sin^2(90° - \mathrm{SZA}) \tag{5}$$

The simulation process commenced with the computation of the direct component of solar irradiance reaching the canopy (edir) and the hemispherical diffuse component (edif), with es and ed representing the solar irradiance spectra for direct and diffuse illumination, respectively.

Subsequently, leveraging insights from (Verhoef and Bach, 2007; Zhou et al., 2017), α_s and α_d, indicating the absorbance of the isolated canopy layer concerning solar and hemispherical diffuse incident flux, were computed utilizing the internal parameters generated during the execution of 4SAIL as a sub-process within PROSAIL-PRO. These parameters encompassed tss (beam transmittance in the sun-target path), tsd (canopy directional-hemispherical transmittance factor), rsd (canopy directional-hemispherical reflectance factor), tdd (canopy bi-hemispherical transmittance factor), and rdd (canopy bi-hemispherical reflectance factor). Consequently, the parameters $\alpha_s x$ and $\alpha_d x$, signifying the canopy absorption for edir and edif, respectively, were also derived by utilizing 4SAIL-generated parameters alongside the parameter dn, which represents the interaction with the background soil. Finally, fAPAR simulation was accomplished by applying the equation:

$$fAPAR = \frac{\sum_{i=0}^{300}(\alpha_{\mathrm{sx}} \cdot \mathrm{edir}[i] + \alpha_{\mathrm{dx}} \cdot \mathrm{edif}[i])}{\sum_{i=0}^{300}(\mathrm{edir}[i] + \mathrm{edif}[i])} \tag{6}$$

The slicing factor was defined within the range of 0 to 300 to compute these values, with consideration given only to wavelengths between 400 and 700 nm.

Moreover, the estimated fAPAR was subsequently utilized to compute Net Primary Production (NPP; gC/m^2/day) using the following equation (FAO, 2020):

$$NPP = S_c \cdot R_s \cdot fAPAR \cdot SM \cdot \varepsilon_{lue} \cdot \varepsilon_p \cdot \varepsilon_t \cdot \varepsilon_{co2} \cdot \varepsilon_{AR} \tag{7}$$

Where:

- $\varepsilon(T, \mathrm{CO}_2)$ is a function derived from S_c represents the scaling factor from Dry Matter Production (DMP) to NPP (0.045).
- R_s denotes the total shortwave incoming radiation (GJ/ha/day) (from ERA5-Land Hourly, 'surface_solar_radiation_downwards').
- ε_p signifies climate efficiency (0.48).
- SM stands for Soil Moisture stress reduction factor (equal to 1).
- ε_{lue} is Light Use Efficiency (LUE) at optimum conditions (2.7 kgDM/GJPA for a C3 crop like Wheat).
- ε_{AR} is the fraction retained after autotrophic respiration (0.5).
- ε_t denotes the normalized temperature effect (Estimated using "ERA5 Daily Avg Temperature" and the Wheat temperature function from (Durgun et al., 2016)).
- ε_{co2} represents the normalized CO_2 fertilization effect. Estimated using the function proposed by Veroustraete (1994):

$$\varepsilon_{\mathrm{CO}_2} = \frac{\mathrm{CO}_2}{\mathrm{CO}_2^{\mathrm{ref}}} \tag{8}$$

Where:

  - CO_2^{ref} represents the CO_2 mixing ratio for the reference year 1833, taken as 281 ppm.
  - CO_2 was taken from the annual 'spatial' average of globally-averaged (CO_2) data from the NOAA-ESRL[1] (414.7 ppm for 2021, 417.07 ppm for 2022).

Following this, a basic linear interpolation was implemented to estimate the cumulative values of NPP at the start and end of each month, aiming to ascertain the total NPP at the conclusion of the

[1] https://gml.noaa.gov/webdata/ccgg/trends/co2/co2_annmean_gl.txt

growing season. Subsequently, the yield was estimated utilizing the equation proposed by Mul and Bastiaanssen (2019):

$$\text{Yield} = \frac{NPP \cdot (AOT \cdot 22.222 \cdot f_c)}{1 - Mc} \cdot HI \quad (9)$$

Where: AOT represents the above over total biomass (0.85), f_c stands for the correlation factor for light use efficiency, Mc is the moisture content in fresh biomass (0.15 for wheat), HI represents the harvest index (taken as 0.4 for Wheat in Gezira estimated by the Hydraulic Research Centre (HRC)), and NPP value here is the seasonal estimate.

2.5. GP models configuration

2.5.1. Model structure

Constructing a GPR model entails crucial decisions regarding the mean function and the kernel function, which essentially govern the behavior of the model. In this study, the mean function was formulated as a simple function that consistently yields the mean value of observations (parameter values). To capture the diverse features of the RTM simulated dataset, we employed the Exponentiated Quadratic covariance kernel provided by TensorFlow-Probability (tfp) (Dillon et al., 2017) to train the GPR models. This process started with defining and initializing the kernel's hyperparameters, including the amplitude (representing the overall variance) and length scale. Moreover, the number of feature dimensions (feature_ndims) was specified as 1, given that the training dataset comprises pairs of parameter values and reflection values. Furthermore, the modeling process took into account observational noise by incorporating the observation_noise_variance parameter of the TensorFlow Gaussian process model. This culminated in three trainable hyperparameters: amplitude, length scale, and observation noise variance.

2.5.2. Model optimization

The optimization process began with the definition of a mini-batch data iterator, with a batch size set to 1000. This iterator was instantiated using TensorFlow's tf.data.Dataset functionality, facilitating efficient data handling and memory usage during training. To introduce randomness and mitigate overfitting, the data was shuffled with a buffer size matching the total size of the training dataset, set at 14,000.

For optimization, the Adaptive Moment Estimation (ADAM) optimizer was selected and configured with a learning rate of 0.001. ADAM was chosen due to its efficacy in dynamically adjusting learning rates for each parameter throughout the training process. As detailed by Kingma and Ba (2014), ADAM stands out for its computational efficiency, low memory footprint, robustness to gradient diagonal rescaling, and suitability for managing high-dimensional data and parameter spaces.

Moreover, a negative log-likelihood (NLL) loss function, denoted as `gp_loss_fn`, was defined. This function encapsulated essential aspects of the Gaussian Process (GP), including the mean function, kernel function, index points (representing reflectance in this context), and observation noise variance. The NLL loss function aimed to minimize the negative log-likelihood of the model, thereby optimizing it to make precise predictions while accommodating the inherent noise in the observations.

These optimization procedures collectively contributed to enhancing the performance and reliability of the Gaussian Process Regression (GPR) model for subsequent analyses. Following this, the model entered a training loop, wherein batched NLL loss values were computed and stored for plotting (`batch_nlls`), while full data NLL values were periodically assessed to comprehensively evaluate model performance (`full_ll`). The training process extended over 10,000 iterations (`nb_iterations`), with updates logged at every 20 iterations (`log_interval`).

To preserve a trained GP model, the trained parameters, including kernel hyperparameters and observation noise variance, were saved, along with the training dataset comprising reflectance values and corresponding parameter values. This dataset facilitated the re-computation of the mean function and subsequent estimation of the standard deviation (STD) when making predictions on new data.

2.5.3. Posterior prediction

For conducting predictions through posterior inference (post-training), the tfp.Distribution GPR class was employed. GPR models were initiated using the trained kernel hyperparameters, observation noise variances, and the training data specific to each model. These GPR models were then used to predict the corresponding parameters (N, fAPAR) and their associated standard deviations (uncertainties) for each row in the acquired Sentinel-2 (S2) bands at the specified date within the study area. Subsequently, these row-level predictions were accurately mapped to their respective positions in the predicted maps (Predicted_parameter_map and Prediction_stdev_map).

3. Results and discussion

3.1. PROSAIL-PRO

3.1.1. Input data sets

Fig. 4 displays how the generated PROSAIL-PRO input variable, a total of 14 of them, as specified in Tables 3 and 4, are interconnected with LAI distribution, as highlighted in 2.3.1.

In these scatter plots, we can observe a clear linear relationship between LAI and the Leaf structure parameter (n), Leaf chlorophyll content (C_{ab}), Leaf carotenoid content (C_{ar}), Leaf water content (C_w), Leaf dry matter (C_m), and Soil brightness (r_{soil}).

The distribution of LAI values follows a Gaussian distribution with most of them centered around LAI = 2, reported sd of 2. The range of LAI was set between 1 to 8, as the expected LAI trend for Wheat is from 0 to 4.5, the range was set in this way to limit the problem of having out-of-range canopy reflectance simulations with low LAI values (less than 0.8) which will eventually affect the trained GPR model's ability in estimating N and fAPAR in early stages of plant development. Furthermore, having very high LAI values for training the model is important for the GPR not to be over-saturated with high values (n the normal limit) during training and for better performance with extreme cases while predicting.

The artefacts observed in the distributions, such as the initial drop in the Cm uniform distribution and the contrasting trends in the uniform distributions of n and rsoil, can be attributed to the co-distribution constraints imposed with high LAI values. Similarly, the decreasing trend in the Gaussian distributions of Cab also arises from these constraints.

After generating the input points, N was calculated using the equations in Section 2.4.1 from the values of LAI and Cp for each input point. This resulted in a range of N values from 2.26 to 45.15 g/m^2. The histogram depicted in Fig. 5 showcases the distribution of N values. In this histogram, each bar represents a specific range of N values, and the height of the bars indicates the frequency of occurrence within each range (with a total sum of 21,000 points). The highest bars in the histogram correspond to the most frequent N values, providing a clear visual representation of the data's distribution.

The majority of N values are concentrated within the range of 5 to 20 g/m^2, as evidenced by the prominent bars in this interval. This range aligns well with the suitability for training a Gaussian Process Regression (GPR) model to predict Wheat's N content, as it encompasses the normal variation in N content within wheat leaves (2.4 to 13.2 g/m^2) during the growing season, as documented in previous research (Berger et al., 2020).

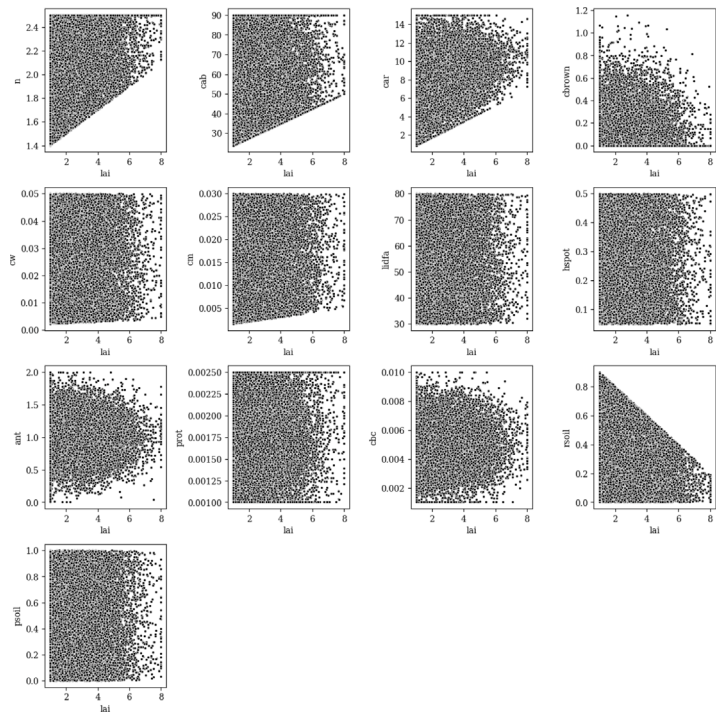

Fig. 4. PROSAIL-PRO input parameters co-distributions.

3.1.2. Distribution of simulated variables

After running PROSAIL-PRO using the generated dataset of 21,000 points, the process concluded with two simulated variables: top of canopy reflectance from 400 to 2500 nm for each input point and simulated fAPAR. In Fig. 6, the statistical characteristics, including the mean, STD, and range, for all the generated reflectance values were highlighted. It is important to note that PROSAIL-PRO is only capable of generating canopy reflectance, the input data (especially the LAI range) was set in a way that ensures the model only simulates reflectance data from the budding growth stage (or the end of the vegetative stage) onwards.

This particular configuration is chosen due to a limitation in RS. From an RS perspective, obtaining valuable information during the early stages of plant growth, especially during the vegetative stage when the canopy is still forming, poses a significant challenge. This challenge remains unless there is access to higher spatial and spectral resolution data.

Subsequently, a statistical test was conducted to assess the potential presence of the ill-posed problem (having two similar reflectance spectrums attributed to different parameter values) within the generated dataset. The result shows that there were no two reflectance profiles found to be entirely identical, even following the application of S2-SRF to derive band values and this can be attributed to two key factors. Firstly, the reasonable selection of parameter ranges during the generation process. These parameter ranges were defined to mimic realistic vegetation scenarios. Secondly, co-distributing the parameters with LAI significantly contributed to the uniqueness of the simulated reflectance values.

Fig. 7 presents a histogram depicting the simulated fAPAR values. Just as explained previously, the fAPAR values are predominantly distributed above the 0.5 threshold to ensure that the trained GPR model can accurately estimate these values, particularly during the intermediate and advanced growth stages of vegetation.

This was driven by a particular consideration: during the early stages of growth, Satellite RS data often faces challenges in capturing accurate canopy reflectance values due to interference from water and background soil reflectance.

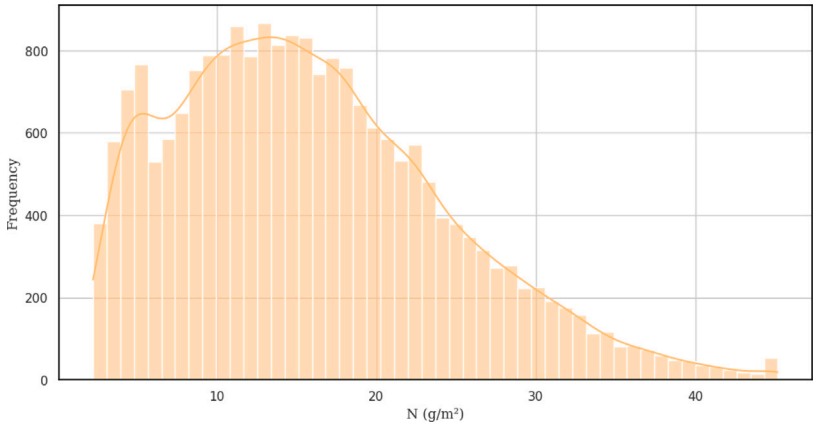

Fig. 5. Above ground nitrogen distribution calculated for each input point using leaf area index and leaf protein content.

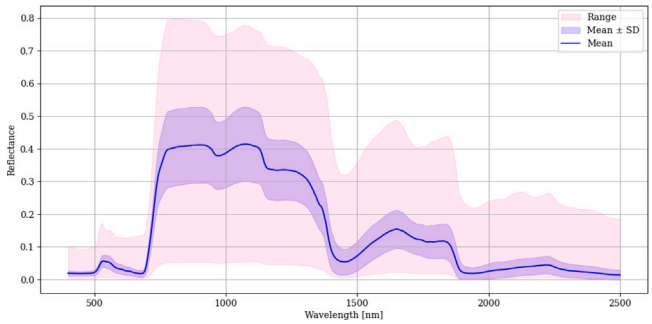

Fig. 6. PROSAIL-PRO simulated reflectance mean, standard deviation, and range for all input points.

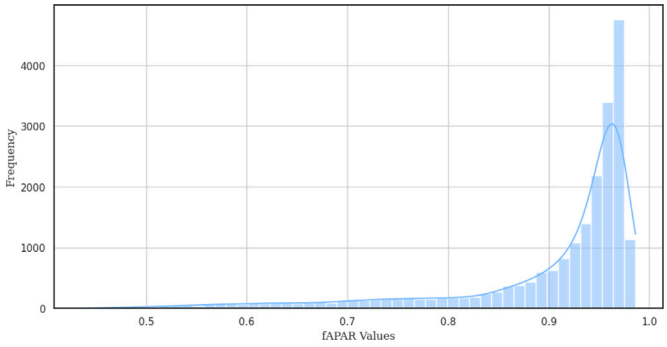

Fig. 7. PROSAIL-PRO simulated fraction of absorbed photosynthetically active radiation distribution.

3.2. GPR models

3.2.1. Training

During the training process, a gradient-based approach, specifically ADAM, was employed to minimize NLL. The complexity of the log marginal likelihood pose a challenge, potentially leading to overfitting of the data. To address this concern, the dataset was partitioned into training (14,000) and validation (7000) sets. The model selection process focused on identifying the best-fit models by evaluating their performance on the validation set, thereby minimizing the risk of overfitting and ensuring robust generalization to unseen data.

The N GPR model demonstrated the most robust performance during training. This outcome can likely be attributed to the Gaussian distribution of N values (depicted in Fig. 5), which is almost centered and well-distributed. In contrast, the distribution of fAPAR values (Fig. 7) is right-skewed.

It is worth mentioning that the normal range of NLL typically falls between zero and positive infinity. However, the occurrence of negative NLL values during the training of the fAPAR model could indicate potential over-fitting to the training data. Negative NLL values are associated with likelihoods derived from probability density functions. This was the case with fAPAR (Fig. 7), given that fAPAR values typically range between 0 and 1. To assess this, it is essential to consider the relative difference between the beginning and end of training. Cross-validation, utilizing the validation data points, helps confirm the significance of this difference.

RMSE and R^2 values for the N GPR model were 3.56 (g/m^2) and 0.66, respectively. For the fAPAR GPR model, these values were 0.044 and 0.82. These metrics collectively indicate that all three models are not over-fitting the data and demonstrate relatively strong performance in their respective tasks.

3.2.2. N prediction

Fig. 8 presents the time series of the Normalized Difference Vegetation Index (NDVI; (Rouse et al., 1974)) computed for the three farms, encompassing all the acquired S2 images during the 2021–22 season (see Table 2). To provide a comprehensive spatial representation, the mean and standard deviation were calculated across all pixels within each farm area.

Interestingly, the NDVI trends across the three farms show a relatively uniform pattern throughout the season. NDVI values increased steadily during the early growth stages and peaked in mid-January, followed by a sharp drop and a subsequent plateau. This decline corresponds with the transition of wheat into the heading and ripening stages, where nitrogen is remobilized from leaves and stems into the grain. Since nitrogen exists in both chlorophyll and protein forms — both closely linked to canopy greenness — the decline in NDVI during this period reflects a physiological reduction in leaf greenness.

Fig. 8 also presents the time series of predicted above-ground nitrogen concentration, derived using the trained N-GPR model based on 10 S2 bands. As with NDVI, the mean and standard deviation were computed across each farm's extent. Although the model showed limited accuracy in early growth stages (seeding to tillering), it performed well from stem elongation onward, aligning with known physiological shifts in nitrogen partitioning.

The motivation for comparing NDVI and nitrogen concentration time series stems from a desire to explore canopy color dynamics across the crop's growth stages and assess how visible greenness patterns relate to nitrogen redistribution. While NDVI alone cannot distinguish among different nutrient management strategies, its temporal behavior can serve as an indirect indicator of crop status when interpreted alongside biochemical indicators like nitrogen concentration.

At first glance, the nitrogen concentration time series exhibits a trend similar to the NDVI curve. This alignment validates the model's ability to track nitrogen uptake and redistribution across stages. As nitrogen remobilizes toward the grain, both NDVI and modeled N concentrations decline. This relationship supports physiological evidence in the literature; for example, Simpson et al. (1983) found that approximately 40% of the grain's nitrogen originates from remobilized leaf nitrogen.

However, while NDVI trends may appear similar between farms (e.g., Farms 1 and 3), this does not imply uniform agronomic conditions. It is important to note that these farms differed in initial nitrogen inputs and land preparation techniques. Moreover, NDVI calculated from just two spectral bands—is known to saturate in high biomass conditions and lacks sensitivity to subtle nutrient variations. In contrast, our nitrogen model utilizes a broader spectral input, enabling more detailed biochemical assessments. This is particularly relevant when considering that a 0.8 tonnes/ha yield difference between Farms 1 and 3, while substantial, is not necessarily evident in NDVI due to its inherent limitations.

Finally, the nitrogen estimates from the GPR model are instantaneous, reflecting canopy status at the time of satellite overpass. The maximum predicted N concentration represents the cumulative uptake from fertilization events, which were uniformly applied from the second to fifth irrigation. Interestingly, nitrogen concentration continued to increase for approximately 10–12 days after the final Urea

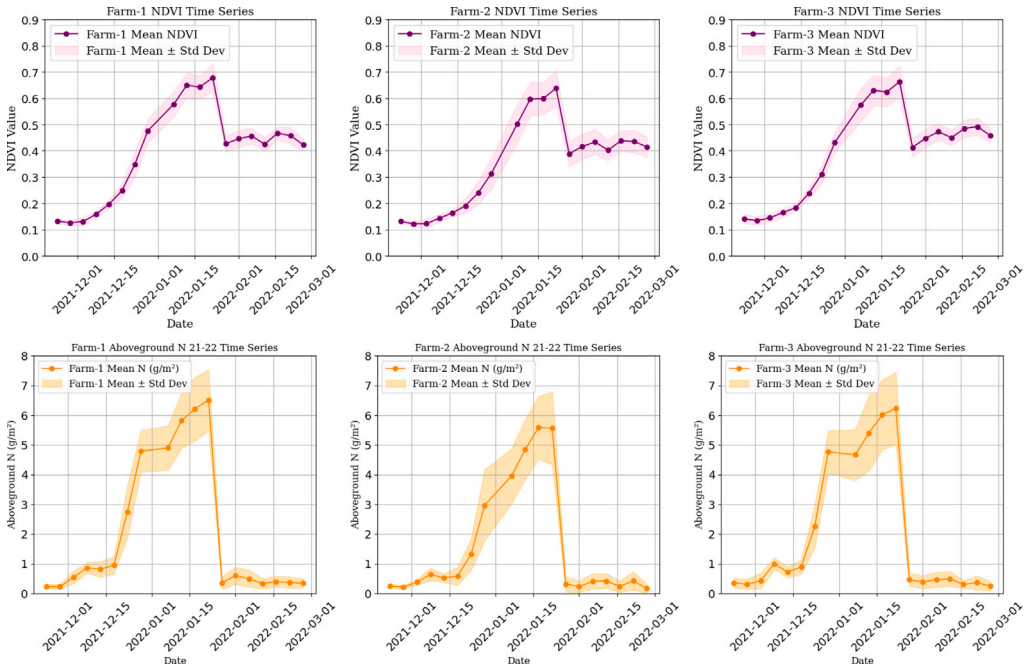

Fig. 8. Normalized difference vegetation index time series for the three farms (top) and predicted above-ground nitrogen time series (bottom).

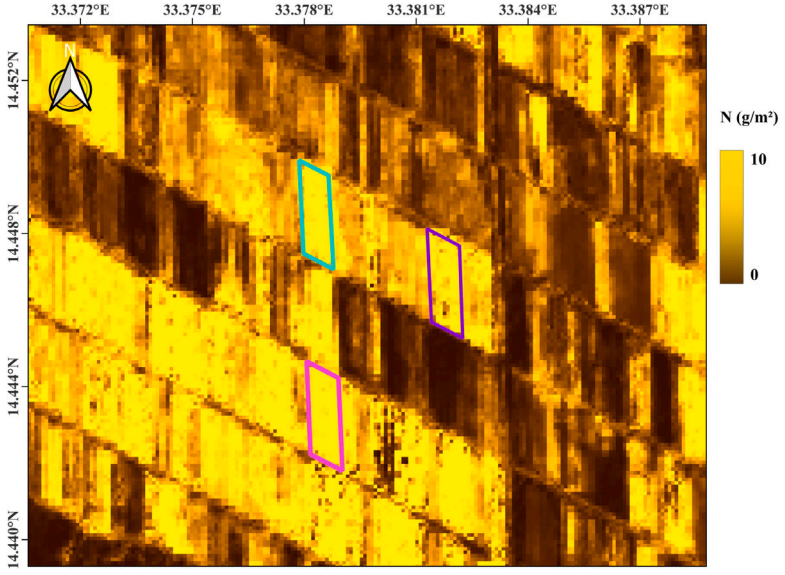

Fig. 9. N-GPR model predicted above ground nitrogen for 2022-01-22.

Table 5
Approximated nitrogen consumption for each farm through the season.

Farm #	Farm-1	Farm-2	Farm-3
Total N consumed (kg/ha)	52.36	52.36	56.6
Predicted mean N content (kg/ha)	65.2	55	60.5

application—highlighting the absorption lag as nitrogen moves from the soil to the plant.

Fig. 9 showcases the above ground *N* concentration predicted by the trained N-GPR using the S2-acquired bands on January 22, 2022.

The appearance of negative values within the predicted map across the study area can be attributed to various factors. Firstly, these negative values are associated with the presence of water bodies, such as the major irrigation canal in the eastern part of the study area and the main and minor canals. Furthermore, areas with built-up infrastructure, such as villages, often exhibit negative and near-zero values. Additionally, the negative values observed in agricultural areas may result from these regions lying fallow during that particular cropping season.

It is important to note that these negative and low values occur due to the GPR model's training solely on canopy reflectance. Such outliers arise from the extrapolation beyond the lowest value that the model was trained on. To gain further insight into areas where the model struggled to interpret reflectance data, we can refer to the generated uncertainty map (STD) of the N-GPR predictions (Fig. 10). This map aids in identifying regions where the model's reflectance predictions may have been less reliable or where unusual values were encountered.

The STD values in the uncertainty map are indicative of the deviation from the mean of the data points used during model training.

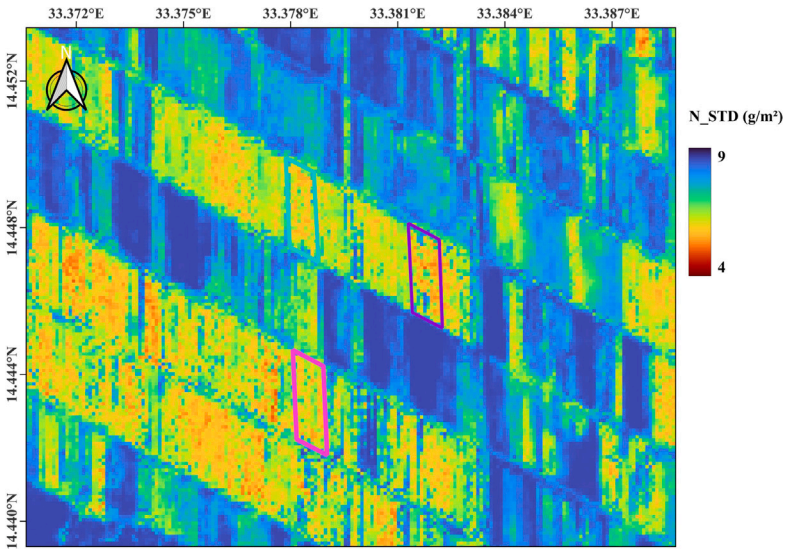

Fig. 10. N-GPR model uncertainties expressed as standard deviation around the mean for 2022-01-22.

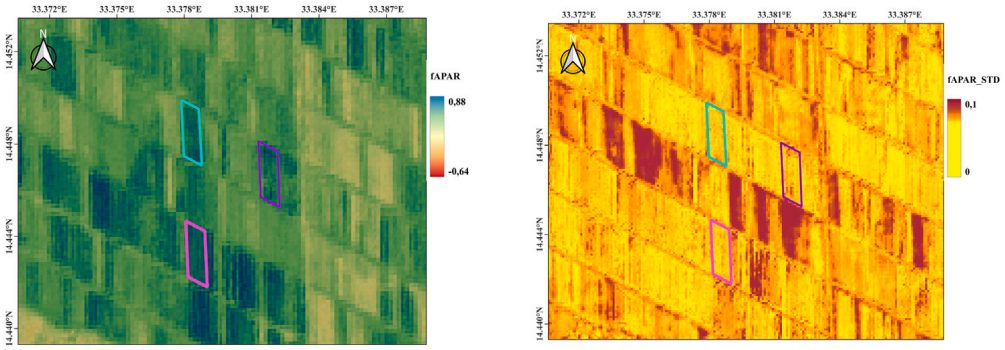

(b) fAPAR-GPR Model Predicted fAPAR for 2022-01-27

(a) fAPAR-GPR Model Uncertainties (Std. Dev) for 2022-01-27

Fig. 11. fAPAR-GPR model outputs on 2022-01-27: (a) Standard deviation representing uncertainty, and (b) predicted fAPAR.

Higher STD values reflect greater uncertainty in the resulting predictions. It is also worth noting that both Figs. 9 and 10 showed similar patterns (very low N values associated with higher uncertainty)

Using the information provided in Table 1, we can calculate the amount of applied N as a percentage of the applied Urea and DAP fertilizers. Given that N represents 46% of the Urea fertilizer and 18% of DAP, the total applied N during the 21–22 season for Farms 1 and 2 was 130.9 kg/ha, and for Farm-3, it was 141.52 kg/ha.

Assuming that only 40% of this applied N was actually utilized by the crops, as suggested by Lassaletta et al. (2014), the consumed N can be estimated as listed in Table 5 below.

Comparing these values to the predicted instantaneous mean N concentrations for each farm on January 22, 2022 (the date with the highest accumulation, which represents the total amount consumed by the plant over the season), reveals an RMSE of 7.9 kg/ha (equivalent to 0.79 g/m^2). This RMSE signifies the deviation between the model's predictions and the observed N concentrations in the field. Notably, despite both Farm-1 and Farm-2 receiving the same amount of nitrogen application, the model predicted different values for them. This difference can be attributed to the additional type of fertilizer (SSP) applied to Farm-1, resulting in an overall higher biomass compared to Farm-2. Due to this difference in biomass, the model was unable to capture the variation in N concentration accurately.

3.2.3. fAPAR prediction

Fig. 11(a) presents the fAPAR-GPR model's uncertainties and Fig. 11(b) illustrates the model's predictions for the S2 product bands on January 27, 2022. Similar to the N-GPR model, the fAPAR-GPR model generated low and negative values for water bodies and built-up areas, accompanied by elevated uncertainty in these predictions.

Notably, both the N-GPR and fAPAR-GPR models attributed negative values to the major canal in the eastern section of the study area (highlighted in red in Fig. 10).

3.2.4. Yield estimation

The bar chart in Fig. 12 compares the actual and predicted yield values across the three farms.

The spatial mean for the predicted yield values was found to be 3.86 tonnes/ha for Farm-1, 3.67 tonnes/ha for Farm-2, and 3.91 tonnes/ha for Farm-3. RMSE for yield estimation was calculated to be 0.54 tonnes/ha. This value can be considered good, especially when considering that the accumulation was done using simple linear interpolation. These estimations further validate the performance of the fAPAR-GPR model in predicting crop yield. It can be seen from the bar chart that there was an overestimation of the yield values for Farms 1 and 2, while for Farm-3 there was a slight underestimation. Since the largest miss-estimation was in Farm-2, it is worth mentioning

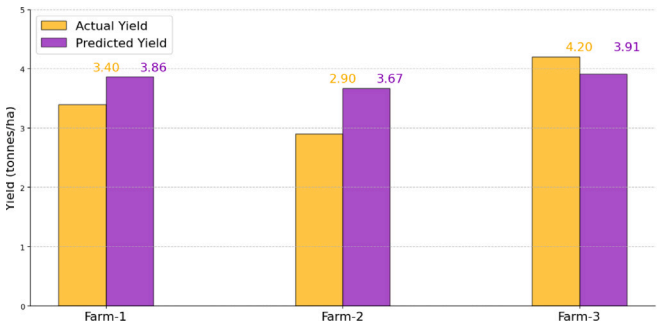

Fig. 12. Predicted yield vs. actual recorded yield for the three farms.

that this could be attributed to the pixels with the high uncertainty (STD) values across Farm-2 borders (Fig. 11(a)). It is also worth noting that the same pixels faced high STD values in *N* estimation (Fig. 10), and this translates that these pixels may be representing a poor performing area because even the end-of-season NDVI values for it were low compared to the rest of the field. And because of that the model was not able to accurately predict fAPAR values for the farm which caused the underestimation and having the largest gap between actual and predicted values.

3.3. Dilution curve

Fig. 13 presents the estimated biomass map for the end of December 2021, with a mean biomass production value of 2 tonnes/ha across the three farms. In the context of the *N* dilution curves, it is important to note that the lower the biomass production value (in tonnes/ha), the steeper the dilution curve becomes, leading to higher critical N% values. From the curves reported by Yao et al. (2021), when the biomass is around 2 tonnes/ha, the critical N% can be approximated as 3% of the biomass.

In consideration of this assumption, the instantaneous critical *N* (in kg/ha) was calculated for all biomass pixels across the three farms. These values were then compared to the predicted above-ground *N* content estimated on December 28, 2021. This comparison provides valuable insights into the implications of the final Urea application, which occurred on January 7, 2022.

The results of this assessment are depicted in Fig. 14. Clearly, Farms 1 and 3 exhibited *N* concentrations above the critical value (the minimum *N* concentration required to ensure growth for that specific biomass value), suggesting a relatively adequate *N* supply. In contrast, Farm-2 appeared to be under significant *N* stress, which could also be the reason for its poor final production.

Notably, despite the relatively small area of the three farms, employing this approach with S2 high resolution enabled the detection of spatial variability, even within these limited areas. Such advisory insights, even if not extraordinarily precise, can contribute to achieving more efficient resource utilization and economic benefits.

4. Models spatiotemporal transferability

The average overall recorded yield in Wad Hilal subzone (Fig. 3) during the 2022–23 season was found to be 2.25 tonnes/ha (with Hegeiliga_Median recording the highest average production of 2.92 tonnes/ha, and BahiEddin3 with the lowest average production of 1.4 tonnes/ha) (Elnour, 2023). RMSE between the actual and the model predicted yield for all the farms was found to be 1.6 tonnes/ha for the field level yield estimation and 1.01 tonnes/ha for the Nimra level estimation with an average overall predicted yield of 3.1 tonnes/ha.

A correlation analysis was conducted between the model's estimations for Nitrogen concentration and the model predicted NPP time series for each farm. The correlation between *N* time series and NPP was found to be higher than the correlation between *N* and fAPAR (Fig. 15), with median correlation values of 0.62 and 0.59 respectively.

Furthermore, the correlation between the median estimated *N* concentration value throughout the season and the actual recorded yield on a field level was found to be 0.7, while the correlation with the average recorded yield on a Nimra level was 0.83. In the first violin plot, which examines the correlation between the simulated Nitrogen timeseries and fAPAR simulation, a notable relationship indicative of the nitrogen impact on photosynthetic activity was observed. This correlation underscores the crucial role of Nitrogen in assessing crop health and productivity. However, what stands out is the subsequent upshift in correlation when transitioning to NPP in the second violin plot. This shift emphasizes the importance of accurate meteorological parameterization when transiting from fAPAR to NPP in a way that helps understanding the nuanced relationship between Nitrogen dynamics and primary productivity.

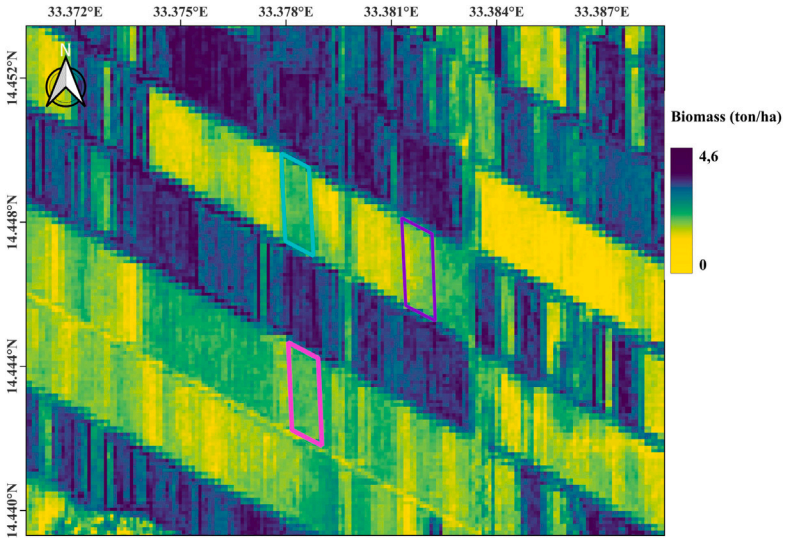

Fig. 13. Biomass estimation for end of December 2021.

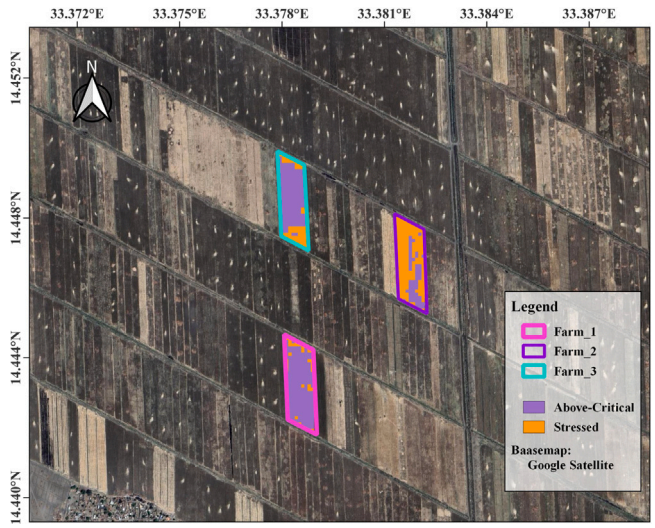

Fig. 14. Nitrogen stress map for the three farms on December 28, 2021.

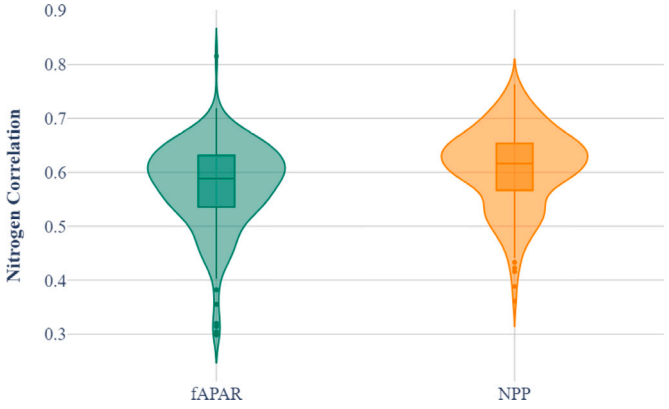

Fig. 15. Nitrogen correlation with the fraction of absorbed photosynthetically active radiation and net primary production.

5. Conclusions

This study demonstrated the value of integrating remote sensing data and machine learning with canopy radiative transfer modeling (PROSAIL-PRO) for estimating crop nitrogen status and biomass throughout the season. Using simulated reflectance data and Sentinel-2 imagery, we trained Gaussian Process Regression (GPR) models to retrieve nitrogen concentration and biomass, achieving RMSE values of 7.9 kg/ha and 0.54 tonnes/ha respectively.

Our analysis emphasized the importance of multiple factors in determining retrieval accuracy, including the quality and distribution of simulated inputs, kernel and mean function choices in GPR, and external conditions such as crop stage and acquisition timing. The models effectively distinguished cropland from non-crop areas, but accurate crop-type identification (e.g., wheat) remained essential for precise biophysical estimations within agricultural zones.

To address the scalability challenges of GPR models in operational settings, we recommend exploring more computationally efficient alternatives, such as linear or polynomial regressions, particularly when sufficient training data are available.

Correlation analysis revealed a strong link between nitrogen dynamics and final yield, underlining the value of including nitrogen as a predictive variable in crop production models to enhance yield estimations.

Finally, the practical application of our workflow in the Gezira irrigation scheme showcased its potential for identifying nitrogen-stressed regions using PROSAIL-driven GPR models and Sentinel-2 imagery. This ability to map nutrient deficiencies through N dilution curves offers promising pathways for more efficient nitrogen resource management and improved precision agriculture practices.

CRediT authorship contribution statement

Mahmoud H. Ahmed: Writing – review & editing, Writing – original draft, Visualization, Software, Methodology, Data curation, Conceptualization. **Sajid Pareeth:** Writing – review & editing, Validation, Supervision, Conceptualization. **Marloes Mul:** Writing – review & editing, Validation, Supervision, Conceptualization.

nret Python package

As part of this study, all functions and scripts used, ranging from the generation of input data points to linking their distribution to Leaf Area Index (LAI) and running them through the PROSAIL-PRO model, have been consolidated into a Python package named “nret” (Nitrogen Retrieval). The NRET package and scripts used for training the Gaussian Process Regression (GPR) model and performing predictions on Sentinel-2 bands are publicly available.[2]

This repository streamlines the entire nitrogen retrieval process, offering a user-friendly and efficient tool for researchers and practitioners in the field. Also, it serves as a valuable resource for those interested in replicating or building upon our research, promoting transparency, and fostering collaboration within the scientific community.

Declaration of competing interest

The authors declare that they have no known competing financial interests or personal relationships that could have appeared to influence the work reported in this paper.

Acknowledgments

This study builds upon the thesis[3] submitted to fulfill the requirements for finishing an MSc degree and can be accessed in . The MSc program was sponsored by the Nuffic-Orange Knowledge program (OKP). The collection of observed data for the 2020–21 season was made possible through the collaboration of the farmer who owns the three farms (Omar El-sir). Additionally, data collection for the 2022–23 season was conducted by HRC as part of the study by Elnour et al. (2024).

Appendix. Methodology flowchart

See Fig. A.16

Data availability

Data will be made available on request. Please contact the corresponding author using the contact details provided in the beginning of this document.

[2] https://github.com/Mahmoud-H97/NRET

[3] https://doi.org/10.25831/tyxh-0t97

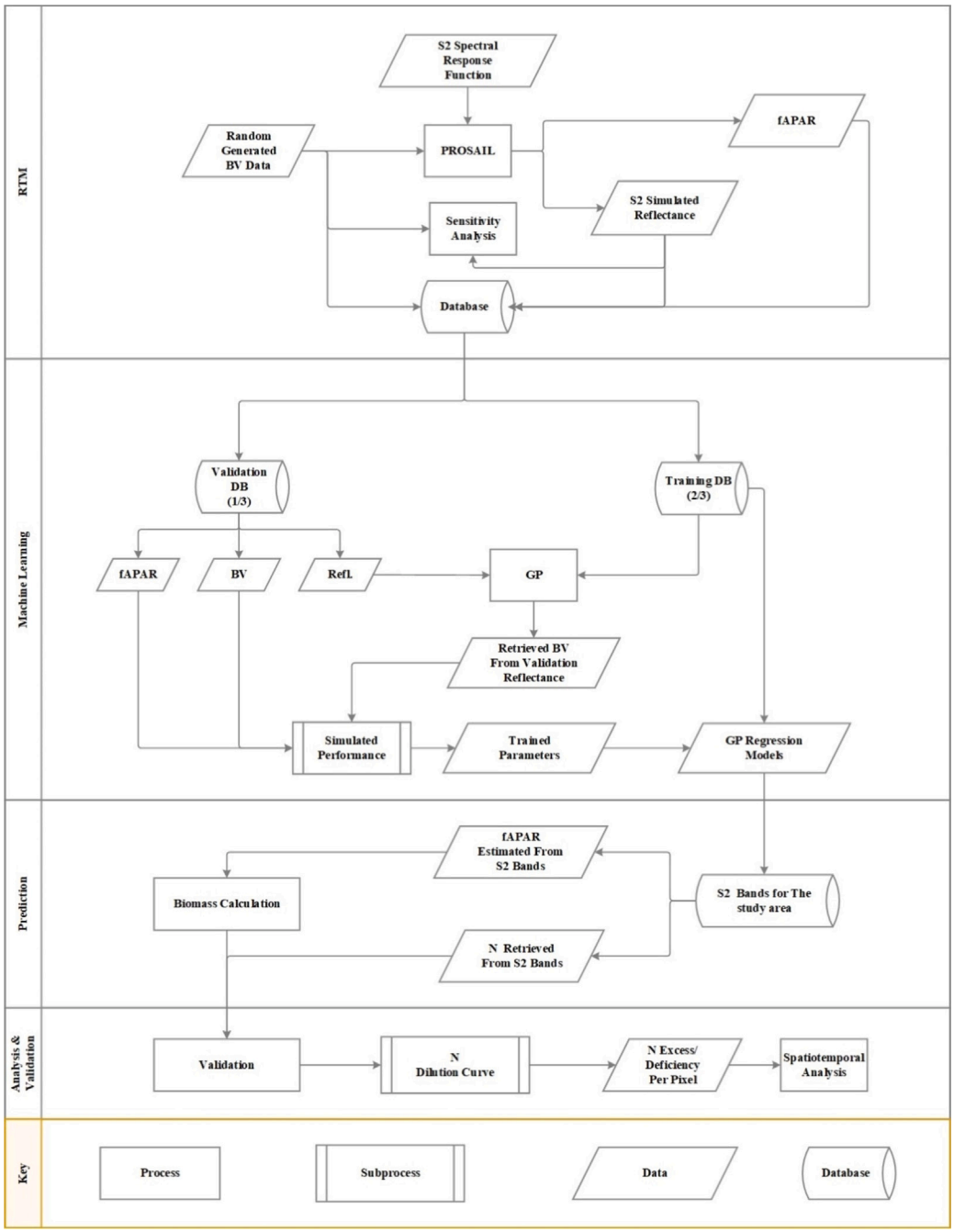

Fig. A.16. Methodology flowchart.

References

Ali, I., Cawkwell, F., Dwyer, E., Barrett, B., Green, S., 2016. Satellite remote sensing of grasslands: from observation to management. J. Plant Ecol. 9 (6), 649–671.

Bacour, C., Baret, F., Béal, D., Weiss, M., Pavageau, K., 2006. Neural network estimation of LAI, fAPAR, fcover and LAI× Cab, from top of canopy MERIS reflectance data: Principles and validation. Remote Sens. Environ. 105 (4), 313–325.

Basso, B., Dumont, B., Cammarano, D., Pezzuolo, A., Marinello, F., Sartori, L., 2016. Environmental and economic benefits of variable rate nitrogen fertilization in a nitrate vulnerable zone. Sci. Total Environ. 545–546, 227–235. http://dx.doi.org/10.1016/j.scitotenv.2015.12.104.

Berger, K., Verrelst, J., Féret, J.B., Hank, T., Wocher, M., Mauser, W., Camps-Valls, G., 2020. Retrieval of aboveground crop nitrogen content with a hybrid machine learning method. Int. J. Appl. Earth Obs. Geoinf. 92, 102174. http://dx.doi.org/10.1016/j.jag.2020.102174.

Berger, K., Wang, Z., Danner, M., Wocher, M., Mauser, W., Hank, T., 2018. Simulation of spaceborne hyperspectral remote sensing to assist crop nitrogen content monitoring in agricultural crops. In: Igarss 2018-2018 IEEE international geoscience and remote sensing symposium. IEEE, pp. 3801–3804. http://dx.doi.org/10.1109/IGARSS.2018.8518537.

Chen, L., Chen, J., Yan, G., Fan, W., Xin, X., Wu, C., Zhao, T., Zhang, S., Li, X., 2017. Remote sensing modelling and parameter inversion. In: The Geographical Sciences During 1986—2015: From the Classics to the Frontiers. Springer, pp. 323–338. http://dx.doi.org/10.1007/978-981-10-1884-8_14.

Congedo, L., 2021. Semi-automatic classification plugin: A python tool for the download and processing of remote sensing images in QGIS. J. Open Source Softw. 6, 3172. http://dx.doi.org/10.21105/joss.03172.

Delloye, C., Weiss, M., Defourny, P., 2018. Retrieval of the canopy chlorophyll content from sentinel-2 spectral bands to estimate nitrogen uptake in intensive winter wheat cropping systems. Remote Sens. Environ. 216, 245–261. http://dx.doi.org/10.1016/j.rse.2018.06.037.

Dillon, J.V., Langmore, I., Tran, D., Brevdo, E., Vasudevan, S., Moore, D., Patton, B., Alemi, A., Hoffman, M., Saurous, R.A., 2017. Tensorflow distributions. http://dx.doi.org/10.48550/arXiv.1711.10604, ArXiv.

Domenzain, L.M., Gómez-Dans, J., Lewis, P., 2019. prosail: Release 2.0.3. 2023, (08/09), http://dx.doi.org/10.5281/zenodo.2574925.

Durgun, Y.Ö., Gobin, A., Gilliams, S., Duveiller, G., Tychon, B., 2016. Testing the contribution of stress factors to improve wheat and maize yield estimations derived from remotely-sensed dry matter productivity. Remote. Sens. 8, 170. http://dx.doi.org/10.3390/rs8030170.

Elkhidir, A., 2019. Eastern Nile Irrigation System Performance Assessment and Options for Improvement Vol. I Sudan Country Report. Report, Eastern Nile Technical Regional Office (ENTRO), Addis Ababa, Ethiopia, URL: https://entrospace.nilebasin.org/entities/publication/f9399dce-0b5a-459c-91eb-200208f8273c/details.

Elnour, R., 2023. Spatial Variation of Land and Water Productivity in Wad Helal Block : Gezira Scheme, Sudan. Delft : IHE Delft Institute for Water Education; 2023, pp. 16–17, URL: http://cdm21063.contentdm.oclc.org/cdm/ref/collection/masters1/id/342899.

Elnour, R., Chukalla, A., Mohamed, Y.A., Verzijl, A., 2024. Multiscale spatial variability in land and water productivity across the gezira irrigation scheme, Sudan. Agricult. Water. Manag. 304, 109082.

Elsayed, E.E., Mohamed, D.M.D., Hassan, A.O., 2019. Economic Assessment of Resource Use in Wheat Production in Gezira Scheme, Sudan (2014/15). Report, University of Gezira, URL: http://dspace.univ-eloued.dz/handle/123456789/4622.

Ennouri, K., Kallel, A., 2019. Remote sensing: An advanced technique for crop condition assessment. Math. Probl. Eng. 2019, 9404565. http://dx.doi.org/10.1155/2019/9404565.

Fan, W., Liu, Y., Xu, X., Chen, G., Zhang, B., 2014. A new FAPAR analytical model based on the law of energy conservation: A case study in China. Sel. Top. Appl. Earth Obs. Remote. Sens., IEEE J. 7, 3945–3955. http://dx.doi.org/10.1109/JSTARS.2014.2325673.

FAO, 2014. The Water-Energy-Food Nexus: A New Approach in Support of Food Security and Sustainable Agriculture. Report, FAO, Rome, Italy, URL: http://www.fao.org/3/a-bl496e.pdf. (Last Accessed on 07 February 2024).

FAO, 2020. WaPOR Database Methodology. Report, FAO, Rome, Italy, URL: https://www.fao.org/documents/card/en/c/ca9894en. (Last Accessed on 07 February 2024).

François, C., Ottlé, C., Olioso, A., Prévot, L., Bruguier, N., Ducros, Y., 2002. Conversion of 400-1100 nm vegetation albedo measurements into total shortwave broadband albedo using a canopy radiative transfer model. Agronomie 22 (6), 611–618. http://dx.doi.org/10.1051/agro:2002033.

Fridgen, J., Kitchen, N., Sudduth, K., Drummond, S.T., Wiebold, W., Fraisse, C., 2003. Management zone analyst (MZA): Software for subfield management zone delineation. Agron. J. 96, http://dx.doi.org/10.2134/agronj2004.1000.

Gao, F., Li, H., 2022. Research on variable rate fertilisation machine based on big data analysis. Acta Agric. Scand. Sect. B — Soil Plant Sci. 72 (1), 225–236. http://dx.doi.org/10.1080/09064710.2021.2008478.

Gascon, F., Bouzinac, C., Thépaut, O., Jung, M., Francesconi, B., Louis, J., Lonjou, V., Lafrance, B., Massera, S., Gaudel-Vacaresse, A., Languille, F., Alhammoud, B., Viallefont, F., Pflug, B., Bieniarz, J., Clerc, S., Pessiot, L., Trémas, T., Cadau, E., De Bonis, R., Isola, C., Martimort, P., Fernandez, V., 2017. Copernicus sentinel-2A calibration and products validation status. Remote. Sens. 9 (6), 584, URL: https://www.mdpi.com/2072-4292/9/6/584.

Gebbers, R., Adamchuk, V., 2010. Precision agriculture and food security. Science327(5967), 828-831. Sci. (New York, N.Y.) 327, 828–831. http://dx.doi.org/10.1126/science.1183899.

Guerif, M., Houlès, V., Frederic, B., 2007. Remote sensing and detection of nitrogen status in crops. Application to precise nitrogen fertilization. In: 4th International Symposium on Intelligent Information Technology in Agriculture. ISIITA 2007, URL: https://hal.inrae.fr/hal-02824189/document.

He, L., 2022. Variable rate technologies for precision agriculture. In: Encyclopedia of Smart Agriculture Technologies. Springer International Publishing, Cham, pp. 1–9. http://dx.doi.org/10.1007/978-3-030-89123-7_34-3.

Hussein, S., Abdelhadi, A., Takeshi, H., 2002. Promotion of participatory water management in the gezira scheme in Sudan. In: Conference Proceedings. FAO International Commission on Irrigation and Drainage) (ICID), pp. 1–4, URL: https://www.ipcinfo.org/fileadmin/user_upload/faowater/docs/ias/paper18.pdf.

Jacquemoud, S., Ustin, S., 2019. Variation due to leaf structural, chemical, and physiological traits. In: Leaf Optical Properties. Cambridge University Press, Cambridge, pp. 170–194. http://dx.doi.org/10.1017/9781108686457.006.

Kang, Y., Özdoğan, M., Zipper, S.C., Román, M.O., Walker, J., Hong, S.Y., Marshall, M., Magliulo, V., Moreno, J., Alonso, L., et al., 2016. How universal is the relationship between remotely sensed vegetation indices and crop leaf area index? A global assessment. Remote. Sens. 8 (7), 597.

Kingma, D.P., Ba, J., 2014. Adam: A method for stochastic optimization. arXiv preprint arXiv:1412.6980.

Kokaly, R.F., 2001. Investigating a physical basis for spectroscopic estimates of leaf nitrogen concentration. Remote Sens. Environ. 75 (2), 153–161. http://dx.doi.org/10.1016/S0034-4257(00)00163-2.

Lassaletta, L., Billen, G., Grizzetti, B., Juliette, A., Garnier, J., 2014. 50 year trends in nitrogen use efficiency of world cropping systems: The relationship between yield and nitrogen input to cropland. Environ. Res. Lett. 105011, 105011. http://dx.doi.org/10.1088/1748-9326/9/10/105011.

Li, Z., Jin, X., Yang, G., Drummond, J., Yang, H., Clark, B., Li, Z., Zhao, C., 2018. Remote sensing of leaf and canopy nitrogen status in winter wheat (Triticum aestivum L.) based on N-PROSAIL model. Remote. Sens. 10 (9), 1463.

Li, Z., Li, Z., Fairbairn, D., Li, N., Xu, B., Feng, H., Yang, G., 2019. Multi-LUTs method for canopy nitrogen density estimation in winter wheat by field and UAV hyperspectral. Comput. Electron. Agric. 162, 174–182.

Mridha, N., Chakraborty, D., Biswal, A., Mitran, T., 2021. Retrieval of crop biophysical parameters using remote sensing. In: Geospatial Technologies for Crops and Soils. Springer Singapore, Singapore, pp. 113–151. http://dx.doi.org/10.1007/978-981-15-6864-0_3.

Mridha, N., Sahoo, R., Kumar, D., Sehgal, V., Krishna, G., Pradhan, S., Gupta, V., 2014. Genetic algorithm based inversion modelling of PROSAIL for retrieval of wheat biophysical parameters from the reflectance data. J. Agric. Phys. 14 (1), 87–95.

Mu, X., Chen, Y., 2021. The physiological response of photosynthesis to nitrogen deficiency. Plant Physiol. Biochem. 158, 76–82. http://dx.doi.org/10.1016/j.plaphy.2020.11.019.

Mul, M., Bastiaanssen, W.G.M., 2019. WaPOR Quality Assessment. Technical Report on the Data Quality of the WaPOR FAO Database Version 1.0. Report, FAO, Rome, Italy and IHE Delft, URL: https://www.fao.org/documents/card/en?details=ca4895en.

Richter, K., Atzberger, C., Vuolo, F., Urso, G.D., 2011. Evaluation of sentinel-2 spectral sampling for radiative transfer model based LAI estimation of wheat, sugar beet, and maize. IEEE J. Sel. Top. Appl. Earth Obs. Remote. Sens. 4 (2), 458–464. http://dx.doi.org/10.1109/JSTARS.2010.2091492.

Rivera, J.P., Verrelst, J., Leonenko, G., Moreno, J., 2013. Multiple cost functions and regularization options for improved retrieval of leaf chlorophyll content and LAI through inversion of the PROSAIL model. Remote. Sens. 5 (7), 3280–3304, URL: https://www.mdpi.com/2072-4292/5/7/3280.

Rouse, J.W., Haas, R.H., Schell, J.A., Deering, D.W., 1974. Monitoring vegetation systems in the great plains with ERTS. NASA Spec. Publ 351 (1), 309.

Rubo, S., Zinkernagel, J., 2022. Exploring hyperspectral reflectance indices for the estimation of water and nitrogen status of spinach. Biosyst. Eng. 214, 58–71. http://dx.doi.org/10.1016/j.biosystemseng.2021.12.008.

Safi, A.R., Karimi, P., Mul, M., Chukalla, A., de Fraiture, C., 2022. Translating open-source remote sensing data to crop water productivity improvement actions. Agricult. Water. Manag. 261, 107373. http://dx.doi.org/10.1016/j.agwat.2021.107373.

Schumann, A.W., 2010. Precise placement and variable rate fertilizer application technologies for horticultural crops. HortTechnology 20 (1), 34–40. http://dx.doi.org/10.21273/HORTTECH.20.1.34.

Science of Agriculture, 2017. Nitrogen in agriculture. 2023, URL: https://scienceofagriculture.org/nitrogen/. (Last accessed on 2023-06-01).

Sehgal, V.K., Chakraborty, D., Sahoo, R.N., 2016. Inversion of radiative transfer model for retrieval of wheat biophysical parameters from broadband reflectance measurements. Inf. Process. Agric. 3 (2), 107–118.

Sehgal, V., Chakraborty, D., Sahoo, R., Pradhan, S., 2013. Canopy radiative transfer models and their inversion for the quantification of vegetation biophysical parameters from remote sensing. ISBN: 978-93-81450-80-2, pp. 181–200.

Simpson, R.J., Lambers, H., Dalling, M.J., 1983. Nitrogen redistribution during grain growth in wheat (Triticum aestivum L.) : IV. Development of a quantitative model of the translocation of nitrogen to the grain. Plant Physiol. 71 (1), 7–14. http://dx.doi.org/10.1104/pp.71.1.7.

Singh, P., Pandey, P.C., Petropoulos, G.P., Pavlides, A., Srivastava, P.K., Koutsias, N., Deng, K.A.K., Bao, Y., 2020. 8 - hyperspectral remote sensing in precision agriculture: present status, challenges, and future trends. In: Hyperspectral Remote Sensing. Elsevier, Hyperspectral Remote Sensing: Theory and Applications, pp. 121–146. http://dx.doi.org/10.1016/B978-0-08-102894-0.00009-7.

Sishodia, R.P., Ray, R.L., Singh, S.K., 2020. Applications of remote sensing in precision agriculture: A review. Remote. Sens. 12 (19), 3136, URL: https://www.mdpi.com/2072-4292/12/19/3136.

Upreti, D., Huang, W., Kong, W., Pascucci, S., Pignatti, S., Zhou, X., Ye, H., Casa, R., 2019. A comparison of hybrid machine learning algorithms for the retrieval of wheat biophysical variables from sentinel-2. Remote. Sens. 11 (5), 481.

Verhoef, W., Bach, H., 2007. Coupled soil–leaf-canopy and atmosphere radiative transfer modeling to simulate hyperspectral multi-angular surface reflectance and TOA radiance data. Remote Sens. Environ. 109 (2), 166–182. http://dx.doi.org/10.1016/j.rse.2006.12.013.

Veroustraete, F., 1994. On the use of a simple deciduous forest model for the interpretation of climate change effects at the level of carbon dynamics. Ecol. Model. 75–76, 221–237. http://dx.doi.org/10.1016/0304-3800(94)90021-3.

Verrelst, J., Dethier, S., Rivera, J.P., Muñoz-Marí, J., Camps-Valls, G., Moreno, J.F., 2016. Active learning methods for efficient hybrid biophysical variable retrieval. IEEE Geosci. Remote. Sens. Lett. 13, 1012–1016.

Verrelst, J., Malenovský, Z., Tol, C., Camps-Valls, G., Gastellu-Etchegorry, J.P., Lewis, P., North, P.R.J., Moreno, J., 2019. Quantifying vegetation biophysical variables from imaging spectroscopy data: A review on retrieval methods. Surv. Geophys. 40, http://dx.doi.org/10.1007/s10712-018-9478-y.

Wang, Z., Skidmore, A.K., Darvishzadeh, R., Wang, T., 2018. Mapping forest canopy nitrogen content by inversion of coupled leaf-canopy radiative transfer models from airborne hyperspectral imagery. Agricult. Forest. Meterol. 253, 247–260.

Weiss, M., Baret, F., 2016. S2ToolBox Level 2 Products: LAI, FAPAR, FCOVER. Report, France's National Research Institute for Agriculture, Food and the Environment (INRA), Paris, France, URL: https://step.esa.int/docs/extra/ATBD_S2ToolBox_L2B_V1.1.pdf. (Last Accessed on 07 February 2024).

Weiss, M., Jacob, F., Duveiller, G., 2020. Remote sensing for agricultural applications: A meta-review. Remote Sens. Environ. 236, 111402. http://dx.doi.org/10.1016/j.rse.2019.111402.

Yao, B., Wang, X., Lemaire, G., Makowski, D., Cao, Q., Liu, X., Liu, L., Liu, B., Zhu, Y., Cao, W., Tang, L., 2021. Uncertainty analysis of critical nitrogen dilution curves for wheat. Eur. J. Agron. 128, 126315. http://dx.doi.org/10.1016/j.eja.2021.126315.

Yeoh, H.H., Wee, Y.C., 1994. Leaf protein contents and nitrogen-to-protein conversion factors for 90 plant species. Food Chem. 49 (3), 245–250.

Zhao, D., Reddy, K.R., Kakani, V.G., Reddy, V.R., 2005. Nitrogen deficiency effects on plant growth, leaf photosynthesis, and hyperspectral reflectance properties of sorghum. Eur. J. Agron. 22 (4), 391–403. http://dx.doi.org/10.1016/j.eja.2004.06.005.

Zhou, G., Liu, X., Zhao, S., Liu, M., Wu, L., 2017. Estimating FAPAR of rice growth period using radiation transfer model coupled with the WOFOST model for analyzing heavy metal stress. Remote. Sens. 9, 424. http://dx.doi.org/10.3390/rs9050424.